A Discontinuous Galerkin Global Shallow Water Model

RAMACHANDRAN D. NAIR, STEPHEN J. THOMAS, AND RICHARD D. LOFT

Scientific Computing Division, National Center for Atmospheric Research, Boulder, Colorado*

(Manuscript received 28 April 2004, in final form 9 September 2004)

ABSTRACT

A discontinuous Galerkin shallow water model on the cubed sphere is developed, thereby extending the transport scheme developed by Nair et al. The continuous flux form nonlinear shallow water equations in curvilinear coordinates are employed. The spatial discretization employs a modal basis set consisting of Legendre polynomials. Fluxes along the element boundaries (internal interfaces) are approximated by a Lax–Friedrichs scheme. A third-order total variation diminishing Runge–Kutta scheme is applied for time integration, without any filter or limiter. Numerical results are reported for the standard shallow water test suite. The numerical solutions are very accurate, there are no spurious oscillations in test case 5, and the model conserves mass to machine precision. Although the scheme does not formally conserve global invariants such as total energy and potential enstrophy, conservation of these quantities is better preserved than in existing finite-volume models.

1. Introduction

High-order methods are becoming increasingly popular in atmospheric modeling. In the last few years, there has been active research in the development of global models based on the spectral-element (SE) method. Spectral elements have a number of computationally attractive features such as high-order accuracy, parallel efficiency, and the ability to accommodate adaptive mesh refinement (AMR). Thus, the SE method has been adopted as the basis of several next-generation atmospheric models (see, e.g., Taylor et al. 1997; Thomas and Loft 2002; Iskandrani et al. 2002; Giraldo and Rosmond 2004; Fournier et al. 2004). Nevertheless, a major disadvantage of SE atmospheric models is a lack of conservation. For climate and atmospheric chemistry applications, conservation of integral invariants such as mass and energy is crucial. Moreover, it is necessary to produce monotonic and positive definite solutions for the transport of water variables and chemical constituents. However, it is not trivial to implement efficient monotonic slope limiters in SE models. There have been several efforts to develop conservative atmospheric models (e.g., Heikes and Randall 1995; Thuburn 1997; Lin and Rood 1997; Bacon et al. 2000), but all of these rely on low-order classical finite-volume methods.

The high-order discontinuous Galerkin (DG) method is ideally suited for atmospheric numerical modeling as it is inherently conservative and can easily incorporate monotonic slope limiters. In addition, it is highly parallel and efficiently handles complex geometries. The DG method may be considered a hybrid approach combining the finite-volume and the finite-element methods, exploiting the merits of both. Discontinuous Galerkin methods became popular following the pioneering work of Cockburn and Shu (1989, 1998) and have been widely adopted in computational fluid dynamics and other engineering applications (e.g., Bassi and Rebay 1997; Remacle et al. 2003). An extensive review of DG methods can be found in Cockburn et al. (2000) and Cockburn and Shu (2001).

In the present paper we extend the DG transport scheme developed by Nair et al. (2005) to a full shallow water model on the cubed sphere in curvilinear coordinates. Recently, Giraldo et al. (2002) developed a global shallow water model using a DG method. However, the basic formulation, spatial discretization, and time integration scheme in our model are quite different from those presented in Giraldo et al. (2002).

The remainder of the paper is organized as follows. Section 2 describes the shallow water equations in cubed-sphere geometry, and section 3 is devoted to the development of a DG shallow water model. Numerical results are given in section 4, followed by conclusions in section 5.

* The National Center for Atmospheric Research is sponsored by the National Science Foundation.

Corresponding author address: Ramachandran D. Nair, Scientific Computing Division, National Center for Atmospheric Research, 1850 Table Mesa Drive, Boulder, CO 80305.
E-mail: rnair@ucar.edu

2. Shallow water model

Here we consider the cubed sphere (computational domain) and the continuous flux form nonlinear shallow water (SW) equations in curvilinear coordinates.

a. Cubed-sphere geometry

As described in Nair et al. (2005), the sphere is decomposed into six identical regions, obtained by central (gnomonic) projection of the faces of the inscribed cube onto the spherical surface (Sadourny 1972; Ronchi et al. 1996). Each of the six local coordinate systems is free of singularities and employs the identical metric terms, creating a nonorthogonal curvilinear coordinate system on the sphere. Nair et al. (2005, hereafter referred to as NTL05), showed that the standard relative error metrics are significantly smaller for an equiangular projection as opposed to equidistant central projection. Here we consider only the equiangular projection.

Let $\mathbf{a}_1$ and $\mathbf{a}_2$ be the covariant base vectors of the transformation between inscribed cube and spherical surface. Let $\mathbf{v} = \mathbf{v}(\lambda, \theta)$ be the horizontal velocity vector specified on the sphere with longitude λ and latitude θ. Then, the components of the covariant vectors are given by $u_1 = \mathbf{v} \cdot \mathbf{a}_1$, $u_2 = \mathbf{v} \cdot \mathbf{a}_2$, and the corresponding contravariant components are expressed as $\mathbf{v} = u^1\mathbf{a}_1 + u^2\mathbf{a}_2$. The metric tensor of the transformation is defined as $G_{ij} \equiv \mathbf{a}_i \cdot \mathbf{a}_j$. Covariant and contravariant vectors are related through the metric tensor G_{ij} such that $u_i = G_{ij}u^j$, $u^i = G^{ij}u_j$, where $G^{ij} = (G_{ij})^{-1}$ and $\mathbf{G} = \det(G_{ij})$. For equiangular coordinates (x^1, x^2), the metric tensor for all six faces of the cube is

$$G_{ij} = \frac{1}{r^4 \cos^2 x^1 \cos^2 x^2} \begin{bmatrix} 1 + \tan^2 x^1 & -\tan x^1 \tan x^2 \\ -\tan x^1 \tan x^2 & 1 + \tan^2 x^2 \end{bmatrix} = \mathbf{A}^{\mathrm{T}}\mathbf{A}, \tag{1}$$

where $r = (1 + \tan^2 x^1 + \tan^2 x^2)^{1/2}$ and $\sqrt{G} = 1/r^3 \cos^2 x^1 \cos^2 x^2$. The matrix $\mathbf{A}$ in (1) can be used for transforming $\mathbf{v}$ with spherical velocity components (u, v) to the local cube-face components (u^1, u^2) and vice versa, as follows (NTL05):

$$\mathbf{A}\begin{bmatrix} u^1 \\ u^2 \end{bmatrix} = \begin{bmatrix} u \\ v \end{bmatrix}, \quad \mathbf{A} = \begin{bmatrix} \cos\theta\, \partial\lambda/\partial x^1 & \cos\theta\, \partial\lambda/\partial x^2 \\ \partial\theta/\partial x^1 & \partial\theta/\partial x^2 \end{bmatrix}. \tag{2}$$

b. Shallow water equations

We consider the flux form shallow water equations in curvilinear coordinates as described in Sadourny (1972). The governing equations for an inviscid flow of a thin layer of fluid in 2D are the horizontal momentum and continuity equations for the height h. Here, h is considered as the depth of the fluid, and it is related to the free surface geopotential height (above sea level) $\Phi = g(h_s + h)$, where h_s denotes height of the underlying mountains, and g is the gravitational acceleration.

In curvilinear coordinates, the continuity and momentum equations for the shallow water system may be written as follows (Sadourny 1972; Arakawa and Lamb 1981; Rančić et al. 1996):

$$\frac{\partial}{\partial t}(\sqrt{G}h) + \frac{\partial}{\partial x^1}(\sqrt{G}u^1h) + \frac{\partial}{\partial x^2}(\sqrt{G}u^2h) = 0, \tag{3}$$

$$\frac{\partial u_1}{\partial t} + \frac{\partial}{\partial x^1}E = -\sqrt{G}u^2(f + \zeta), \tag{4}$$

$$\frac{\partial u_2}{\partial t} + \frac{\partial}{\partial x^2}E = -\sqrt{G}u^1(f + \zeta), \tag{5}$$

where

$$E = \Phi + \frac{1}{2}(u_1u^1 + u_2u^2), \quad \zeta = \frac{1}{\sqrt{G}}\left[\frac{\partial u_2}{\partial x^1} - \frac{\partial u_1}{\partial x^2}\right],$$

$f = 2\omega \sin\theta$ is the Coriolis parameter, and ω is the rotation rate of the earth.

The six local Cartesian coordinate systems (x^1, x^2) that span the surface of the sphere are based on equiangular central projection (NTL05) in such a way that $x^1 = x^1(\lambda, \theta)$, $x^2 = x^2(\lambda, \theta)$, and $-\pi/4 \le x^1, x^2 \le \pi/4$.

The system (3)–(5) may be expressed in the following flux form:

$$\frac{\partial}{\partial t}\mathbf{U} + \frac{\partial}{\partial x^1}\mathbf{F}_1(\mathbf{U}) + \frac{\partial}{\partial x^2}\mathbf{F}_2(\mathbf{U}) = \mathbf{S}(\mathbf{U}) \tag{6}$$

where $\mathbf{U} = [\sqrt{G}h, u_1, u_2]^{\mathrm{T}}$, $\mathbf{F}_1 = [\sqrt{G}hu^1, E, 0]^{\mathrm{T}}$ $\mathbf{F}_2 = [\sqrt{G}hu^2, 0, E]^{\mathrm{T}}$, with the source terms $\mathbf{S} = [0, \sqrt{G}u^2(f + \zeta), -\sqrt{G}u^1(f + \zeta)]^{\mathrm{T}}$.

3. Discontinuous Galerkin formulation

For simplicity, we proceed with a scalar component of (6) to describe the DG discretization:

$$\frac{\partial U}{\partial t} + \nabla \cdot \mathcal{F}(U) = S(U), \quad \text{in} \quad D \times (0, T), \tag{7}$$

for all $(x^1, x^2) \in D$ with initial condition $U_0(x^1, x^2) = U(x^1, x^2, t = 0)$. In (7), $\mathcal{F} = (F_1, F_2)$ is the flux function, $U = U(x^1, x^2, t)$, and $\nabla \equiv (\partial/\partial x^1, \partial/\partial x^2)$ is the gradient operator. Equation (7) includes a source term $S(U)$, otherwise it is the same as Eq. (14) considered in NTL05.

The computational domain $\mathcal{D}$ is the surface of the cubed sphere, spanning six identical nonoverlapping subdomains (faces) such that $\mathcal{D} = \cup_{\nu=1}^{6}\Omega^{\nu}$. Therefore, it is only necessary to consider the discretization for a single subdomain Ω^{ν}, and the procedure can be analogously extended to the remaining subdomains (hereafter, the superscript ν has been dropped). Consider a subdomain Ω that is partitioned into $N_e \times N_e$ rectangular nonoverlapping elements Ω_{ij}; $i, j = 1, 2, \ldots, N_e$, such that

$$\Omega_{ij} = [(x^1, x^2)|x^1 \in (x^1_{i-1/2}, x^1_{i+1/2}), x^2 \in (x^2_{j-1/2}, x^2_{j+1/2})] \tag{8}$$

Thus, the total number of elements on the cubed sphere is $M = 6 \times N_e^2$. The size of an element Ω_{ij} is determined by $\Delta x_i^1 = (x_{i+1/2}^1 - x_{i-1/2}^1)$ and $\Delta x_j^2 = (x_{j+1/2}^2 - x_{j-1/2}^2)$ in the x^1 and x^2 directions, respectively. For $t > 0$, consider an element Ω_{ij} in the partition of Ω,and an approximate solution $U_h(x^1, x^2, t)$ belongs to the finite dimensional space $\mathcal{V}_h(\Omega)$. Multiplication of (7) by a test function $\varphi_h(x^1, x^2) \in \mathcal{V}_h$ and integration over the element Ω_{ij}^v results in a weak Galerkin formulation of the problem:

$$\frac{\partial}{\partial t}\int_{\Omega_{ij}} U_h(x^1, x^2, t)\varphi_h(x^1, x^2)\, d\Omega - \int_{\Omega_{ij}} \mathcal{F}[U_h(x^1, x^2, t)] \cdot \nabla\varphi_h(x^1, x^2)\, d\Omega + \int_{\partial\Omega_{ij}} \mathcal{F}[U_h(x^1, x^2, t)] \cdot \mathbf{n}\varphi_h(x^1, x^2)\, ds = \int_{\Omega_{ij}} S[U_h(x^1, x^2, t)]\, \varphi_h(x^1, x^2)\, d\Omega, \tag{9}$$

where $\mathbf{n}$ is the outward-facing unit normal vector on the element boundary $\partial\Omega_{ij}$.

a. Flux terms

Along the boundaries of an element (internal interfaces) $\partial\Omega_{ij}$, the function U_h is discontinuous and the boundary integral [third term in (9)] is not uniquely defined. Therefore, the analytic flux $\mathcal{F}(U_h) \cdot \mathbf{n}$ in (9) must be replaced by a numerical flux $\hat{\mathcal{F}}(U_h^-, U_h^+)$. The numerical flux resolves the discontinuity along the element edges and provides the only mechanism by which adjacent elements interact. A variety of numerical fluxes are available to approximate the solution of the resulting Riemann problem (Cockburn and Shu 2001). For simplicity, the Lax–Friedrichs numerical flux as considered in NTL05 is chosen for the present study, given by

$$\hat{\mathcal{F}}(U_h^-, U_h^+) = \frac{1}{2}\{[\mathcal{F}(U_h^-) + \mathcal{F}(U_h^+)] \cdot \mathbf{n} - \alpha(U_h^+ - U_h^-)\}, \tag{10}$$

where U_h^- and U_h^+ are the left and right limits of the discontinuous function U_h evaluated at the element interface, α is the upper bound for the absolute value of eigenvalues of the flux Jacobian $\mathcal{F}'(U)$ in the direction $\mathbf{n}$.

For the shallow water system (6), the values of α in x^1 and x^2 directions are defined as follows (see appendix A for derivations):

$$\alpha^1 = \max(|u^1| + \sqrt{\Phi\, G^{11}}),$$
$$\alpha^2 = \max(|u^2| + \sqrt{\Phi\, G^{22}}), \tag{11}$$

where the maximum value is local to the element Ω_{ij}. Treatment of flux terms and vector quantities at the cube-face edges needs special attention, and it is discussed in NTL05. We proceed with the spatial discretization as follows.

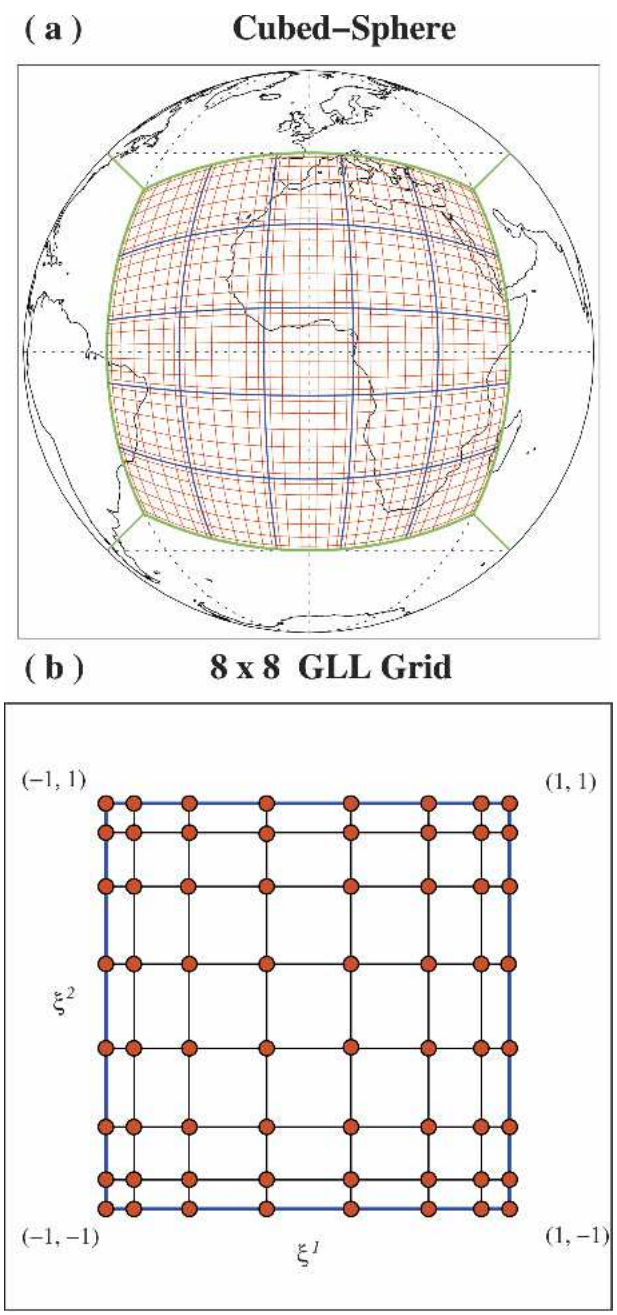

FIG. 1. (a) A cubed sphere consisting of 25 elements ($N_e = 5$) on a face is shown. With this configuration 150 elements are required to span the surface of the sphere ($6 \times N_e^2 = 150$). Each element contains 8×8 GLL points. (b) A schematic illustration of a reference element with 8×8 GLL points. Each element on the cubed sphere as shown in (a) is mapped onto the reference element $[-1, 1] \otimes [-1, 1]$.

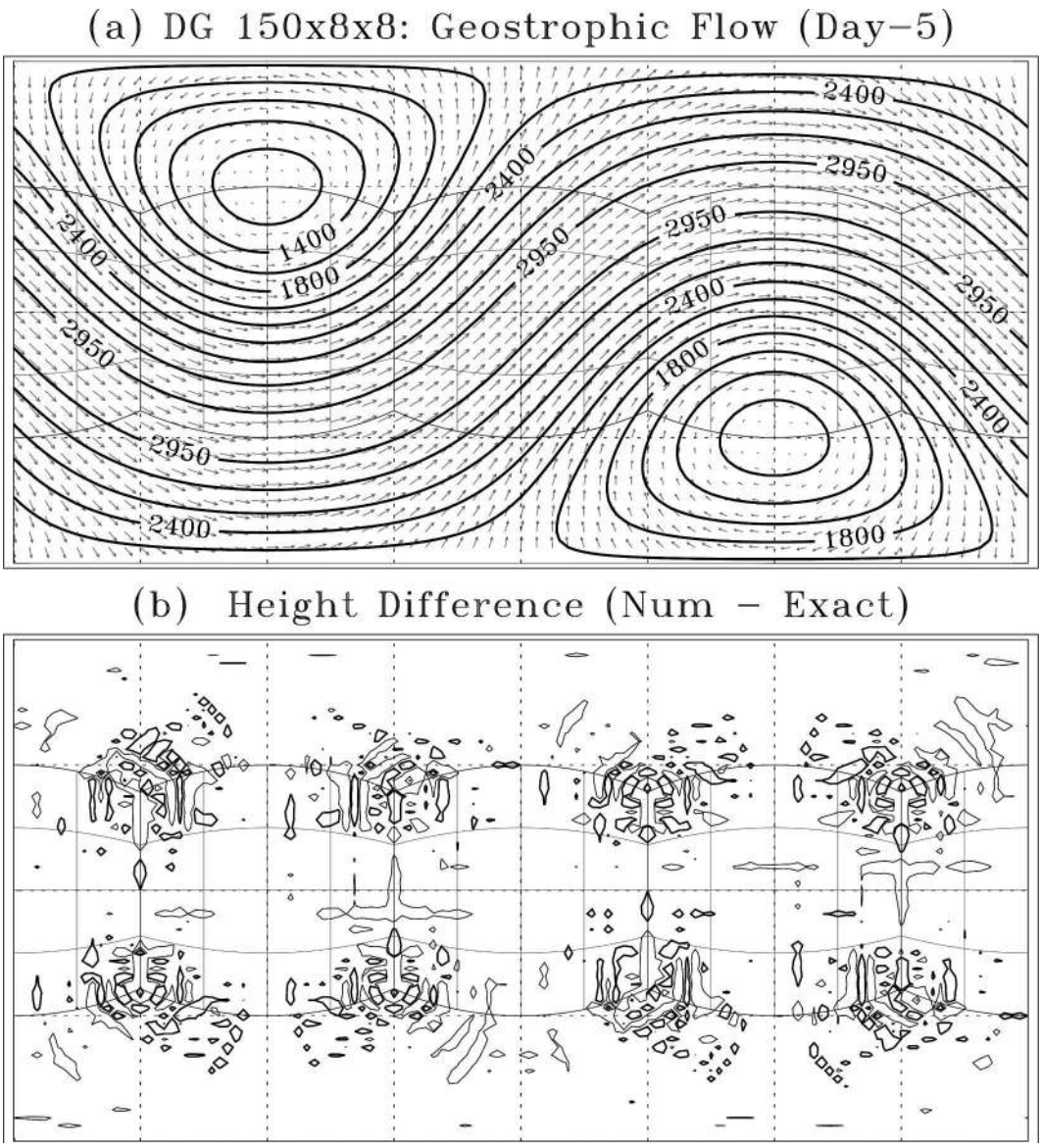

FIG. 2. (a) Numerical solution and (b) height error for SW test case 2. A cubed sphere with 150 elements, each of which contains 8×8 GLL points, is used for numerical integrations. The contour values for difference height field (in meters) are -8×10^{-6} (thin lines) and 8×10^{-6} (thick lines).

b. Discretization

For each element Ω_{ij}, define the local variables

$$\xi^1 = \frac{2(x^1 - x_i^1)}{\Delta x_i^1}, x_i^1 = (x_{i+1/2}^1 + x_{i-1/2}^1)/2$$

$$\xi^2 = \frac{2(x^2 - x_j^2)}{\Delta x_j^2}, x_j^2 = (x_{j+1/2}^2 + x_{j-1/2}^2)/2$$

By using above relations, an element Ω_{ij} is mapped onto the reference element $\Omega_{ij} \equiv [-1, 1] \otimes [-1, 1]$. Figure 1 shows the cubed sphere with 5×5 elements on each face ($N_e = 5$). Note that for clarity, elements on a single face are displayed, and each element is mapped onto a reference element Ω_{ij} shown in the lower panel.

An important aspect of the DG discretization is the choice of an appropriate set of basis functions (polynomials) that span $\mathcal{V}_h$. Even though DG solutions do not rely on the choice of basis, the computational efficiency of the DG scheme is very much dependent on the basis. For example, if we choose the set of Legendre polynomials of degree up to N, $\mathcal{B} = \{P_\ell(\xi), \ell = 0, \ldots, N\}$ as the basis set, then the mass matrix associated with discretization of (9) is diagonal because of the L^2 orthogonality of the Legendre polynomials. Consequently, explicit time integration can be performed without inverting or

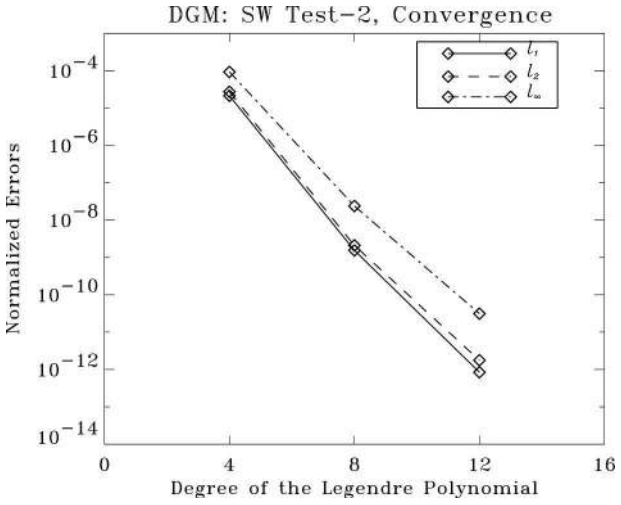

FIG. 3. Convergence of high-order DG scheme for SW test case 2. Normalized ℓ_1, ℓ_2 and ℓ_∞, height errors as a function of Legendre polynomial degree. The results are shown after 5 days of integration on grids with fixed number of total elements ($M = 54$) but varying polynomial degree.

lumping the mass matrix. This type of basis is known as a *modal* basis and greatly simplifies p refinement (for AMR applications) and elementwise slope limiting (for monotonic solutions). An alternative approach is a *nodal* basis where the basis set is constructed using Lagrange–Legendre polynomials with roots at Gauss–Lobatto quadrature points (Giraldo et al. 2002). The choice of a particular type of basis is problem dependent, and their relative merits are discussed in Karniadakis and Sherwin (1999).

We choose $\mathcal{B}$ as the basis set, as in NTL05. In the two-dimensional (2D) (ξ^1, ξ^2) coordinate system, the test function (φ_h) as well as the approximate solution $U_h(x^1(\xi^1), x^2(\xi^2), t)$ are expanded in terms of tensor-product functions from $\mathcal{B}$. Thus,

$$U_{ij}(\xi^1, \xi^2, t) = \sum_{\ell=0}^{N} \sum_{m=0}^{N} \hat{U}_{ij\ell m}(t) P_\ell(\xi^1) P_m(\xi^2) \quad \text{for} \quad -1 \le \xi^1, \xi^2 \le 1, \tag{12}$$

where

$$\hat{U}_{ij\ell m}(t) = \frac{(2\ell + 1)(2m + 1)}{4} \int_{-1}^{1} \int_{-1}^{1} U(\xi^1, \xi^2, t)\, P_\ell(\xi^1)\, P_m(\xi^2) d\xi^1\, d\xi^2. \tag{13}$$

The weak formulation (9) is simplified by mapping the elements onto the reference element and utilizing (12) together with the properties of Legendre polynomials. The final approximation of (7) takes the form

$$\frac{d}{dt} \hat{U}_{ij\ell m}(t) = \frac{(2\ell + 1)(2m + 1)}{2\Delta x_i^1 \Delta x_j^2} [I_Q + I_F + I_G + I_S], \tag{14}$$

where I_F and I_G are flux integrals in x^1 and x^2 directions, and I_Q and I_S are the integrals corresponding to the gradient and source terms in (9), respectively. The explicit forms of the integrals I_Q, I_F, and I_G are analogous to the corresponding integrals given in NTL05, and the integral I_S is defined as

$$I_S = \frac{\Delta x_i^1 \Delta x_j^2}{2} \int_{-1}^{1} \int_{-1}^{1} \{S[U(\xi^1, \xi^2, t)]\, P_\ell(\xi^1)\, P_m(\xi^2)\}\, d\xi^1\, d\xi^2. \tag{15}$$

Equation (14) consists of both surface and boundary integrals. These integrals are computed with an accurate Gauss–Lobatto–Legendre (GLL) quadrature rule that is exact for polynomials of degree $2N + 1$.

The semidiscretized Eq. (14) is an ordinary differential equation; for the shallow water system it takes the following form:

$$\frac{d}{dt} \mathbf{U} = \mathbf{L}(\mathbf{U}) \quad \text{in} \quad (0, T). \tag{16}$$

For time integration, ODE (16) must be solved. Total variation-diminishing Runge–Kutta (TVD-RK) schemes do not introduce spurious oscillations for smooth problems and are widely used for DG methods (Cockburn and Shu 1998). In particular, a TVD scheme preserves strong stability, implying that no new local maxima or minima will be generated (see Gottlieb et al. 2001). The DG model developed by Giraldo et al. (2002) employs a non-TVD fourth-order RK scheme combined with a Boyd–Vandeven spatial filter. For the present study we use the TVD scheme considered in NTL05, without a limiter or a filter. The third-order TVD-RK scheme can be written as follows for (16):

$$\begin{aligned} \mathbf{U}^{(1)} &= \mathbf{U}^n + \Delta t\, \mathbf{L}(\mathbf{U}^n) \\ \mathbf{U}^{(2)} &= \frac{3}{4} \mathbf{U}^n + \frac{1}{4} \mathbf{U}^{(1)} + \frac{1}{4} \Delta t\, \mathbf{L}(\mathbf{U}^{(1)}) \\ \mathbf{U}^{n+1} &= \frac{1}{3} \mathbf{U}^n + \frac{2}{3} \mathbf{U}^{(2)} + \frac{2}{3} \Delta t\, \mathbf{L}(\mathbf{U}^{(2)}) \end{aligned} \tag{17}$$

where the superscripts n and $n + 1$ denote time levels t and $t + \Delta t$, respectively. However, if the solution contains strong shocks or discontinuities, oscillations will appear, which leads to nonlinear instabilities. To avoid spurious oscillations in the numerical solution, a slope limiter can be applied after each stage of the Runge–Kutta time integration (17).

4. Numerical results with some test cases

Our DG scheme has been extensively tested using various initial conditions. Williamson et al. (1992, hereafter referred to as W92), proposed a suite of standard tests for the shallow water equations on the sphere. These idealized tests of varying complexity include

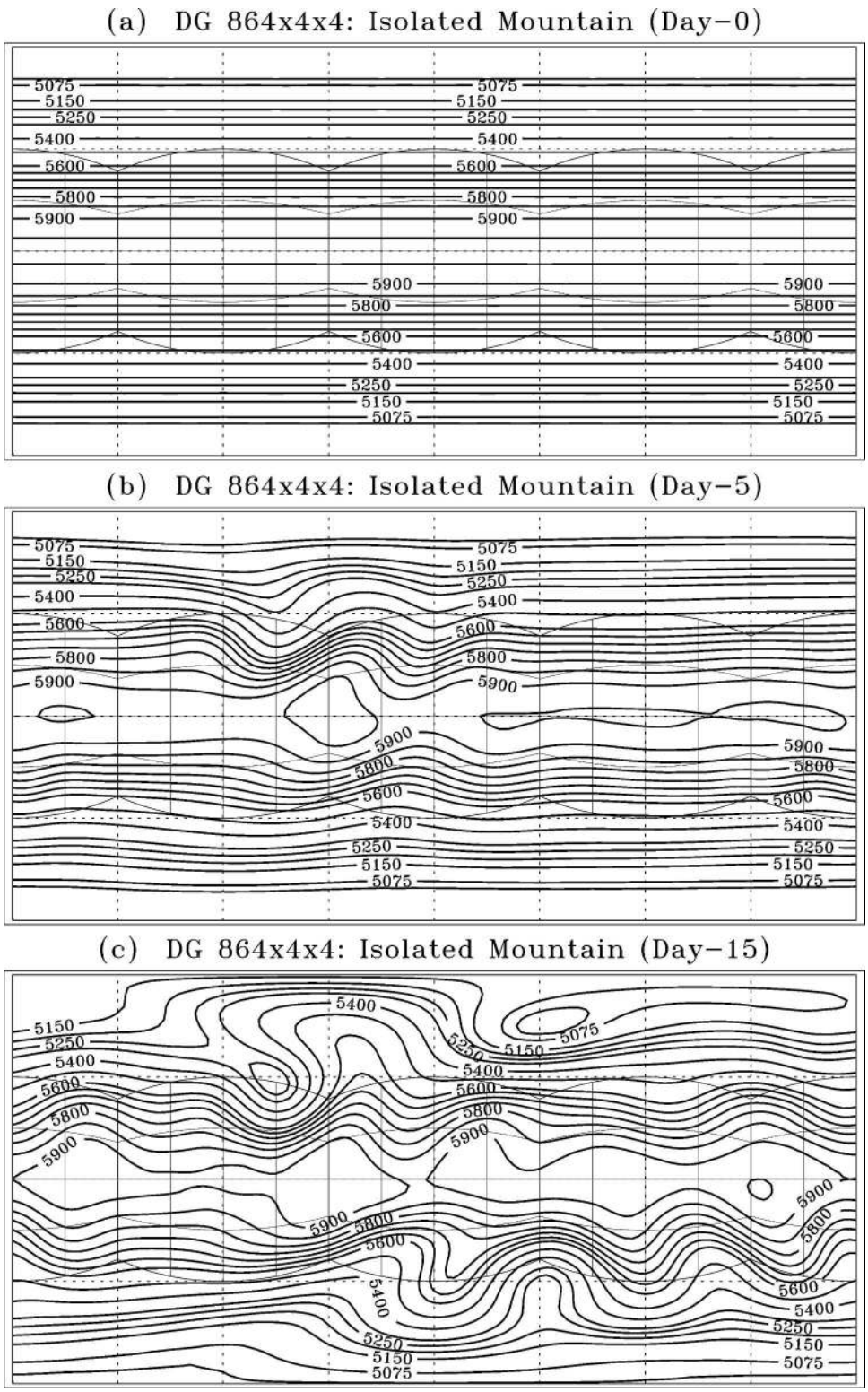

FIG. 4. Numerical solution of SW test case 5, zonal flow impinging a mountain, on an $864 \times 4 \times 4$ grid. (a) The initial height and the numerical solution (height) after (b) 5 and (c) 15 days of integration.

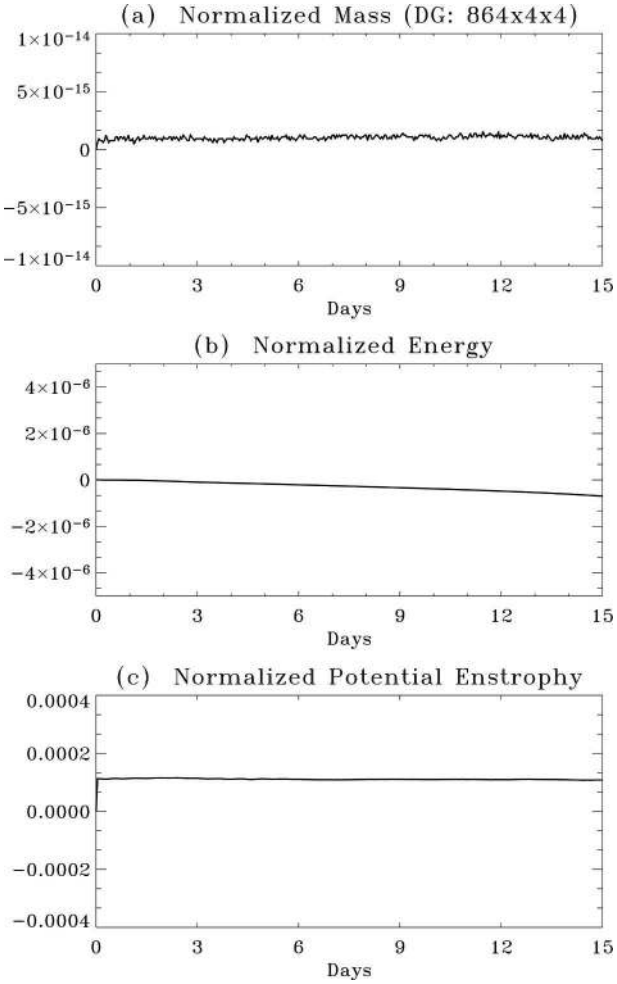

FIG. 5. Time traces of normalized integral invariants for SW test case 5: (a) total mass, (b) total energy, and (c) potential enstrophy.

experiments with north–south symmetry, balanced steady-state flows, and extreme gradients. In addition to the W92 tests, we also consider a test proposed by McDonald and Bates (1989). All of the experiments discussed here utilize the TVD Runge–Kutta time integration scheme (17) without a filter or limiter. We have employed a variety of grid systems with $M \times N_g \times N_g$ grid points, where M is the total number of elements ($M = 6N_e^2$) on the cubed sphere and each element consists of $N_g \times N_g$ Gauss–Lobatto–Legendre points. Numerical solutions produced with the DG scheme on the cubed sphere are bilinearly interpolated onto a 128×65 longitude–latitude grid (approximately equal to the T42 resolution) for visualization.

Results for the solid-body rotation experiment proposed in W92 are reported in NTL05 and will not be considered here.

a. Steady-state geostrophic flow

First, we consider test case 2 in W92, which is a steady-state solution of the full nonlinear SW equations. The wind field is uniform as in the solid-body rotation case and the equations are geostrophically balanced during the time evolution. The initial velocity and height fields are

$$u = u_0(\cos\alpha_0 \cos\theta + \sin\alpha_0 \cos\lambda \sin\theta),$$

$$v = -u_0 \sin\alpha_0 \sin\lambda,$$

$$g h = g h_0 - \frac{u_0}{2}(2a\omega + u_0)(\sin\theta \cos\alpha_0 - \cos\lambda \cos\theta \sin\alpha_0)^2$$

where a is the earth's radius, $u_0 = 2\pi a/(12 \text{ days})$, and $gh_0 = 2.94 \times 10^4 \text{ m}^2 \text{ s}^{-2}$.

We have chosen the flow orientation parameter $\alpha_0 = \pi/4$, making the test more challenging on the cubed sphere. Figure 2a shows the height and wind fields after 5 days of integration. The difference of the height fields (numerical minus exact) is displayed in Fig. 2b. The maximum error is $O(10^{-6})$ m, and the largest errors appear to be clustered around the cube vertices. The experiment was performed on a $150 \times 8 \times 8$ grid (i.e., $N_e = 5$, $N_g = 8$ as shown in Fig. 1) with time step $\Delta t = 36$ s. Figure 3 shows the convergence of the standard error norms ℓ_1, ℓ_2 and ℓ_∞, for test case 2, with varying degree of the Legendre polynomials. This clearly shows the exponential convergence of the DG scheme.

b. Zonal flow over an isolated mountain

The second experiment we consider is test case 5 in W92, zonal flow over an isolated mountain. This test is particularly useful for studying the effectiveness of the scheme in conserving integral invariants such as mass, total energy, and potential enstrophy. It consists of a zonal flow impinging on a mountain, and no analytic solution is known for this test. The center of the mountain is located at $(3\pi/2, \pi/6)$ with height $h_s = 2000\,(1 - r/R)$ m, where $R = \pi/9$ and $r^2 = \min[R^2, (\lambda - 3\pi/2)^2 + (\theta - \pi/6)^2]$. The wind velocity and height fields are the same as in the previous case with $\alpha_0 = 0$, $gh_0 = 5960 \text{ m}^2 \text{ s}^{-2}$, and $u_0 = 20 \text{ m s}^{-1}$.

Initial conditions and the numerical results on a $864 \times 4 \times 4$ grid are shown in Fig. 4. Figures 4b and 4c display the numerical results after 5 and 15 days of integrations, respectively. The numerical solutions are smooth and do not exhibit spurious oscillations, and they appear very similar to the high-resolution spectral T213 solutions shown in Jakob-Chien et al. (1995). However, the spectral solutions exhibit spurious oscillations in the vicinity of the mountain at all resolutions. We have repeated the experiment using a "high order" grid ($N = 8$) with 54 elements, and this configuration approximately compares with that of Giraldo et al. (2002), who have used 60 elements. Displays of the height, zonal, and meridional components of the velocity fields after 10 days of integration are shown later (in Fig 6). Giraldo et al. (2002) exhibit spurious oscillations

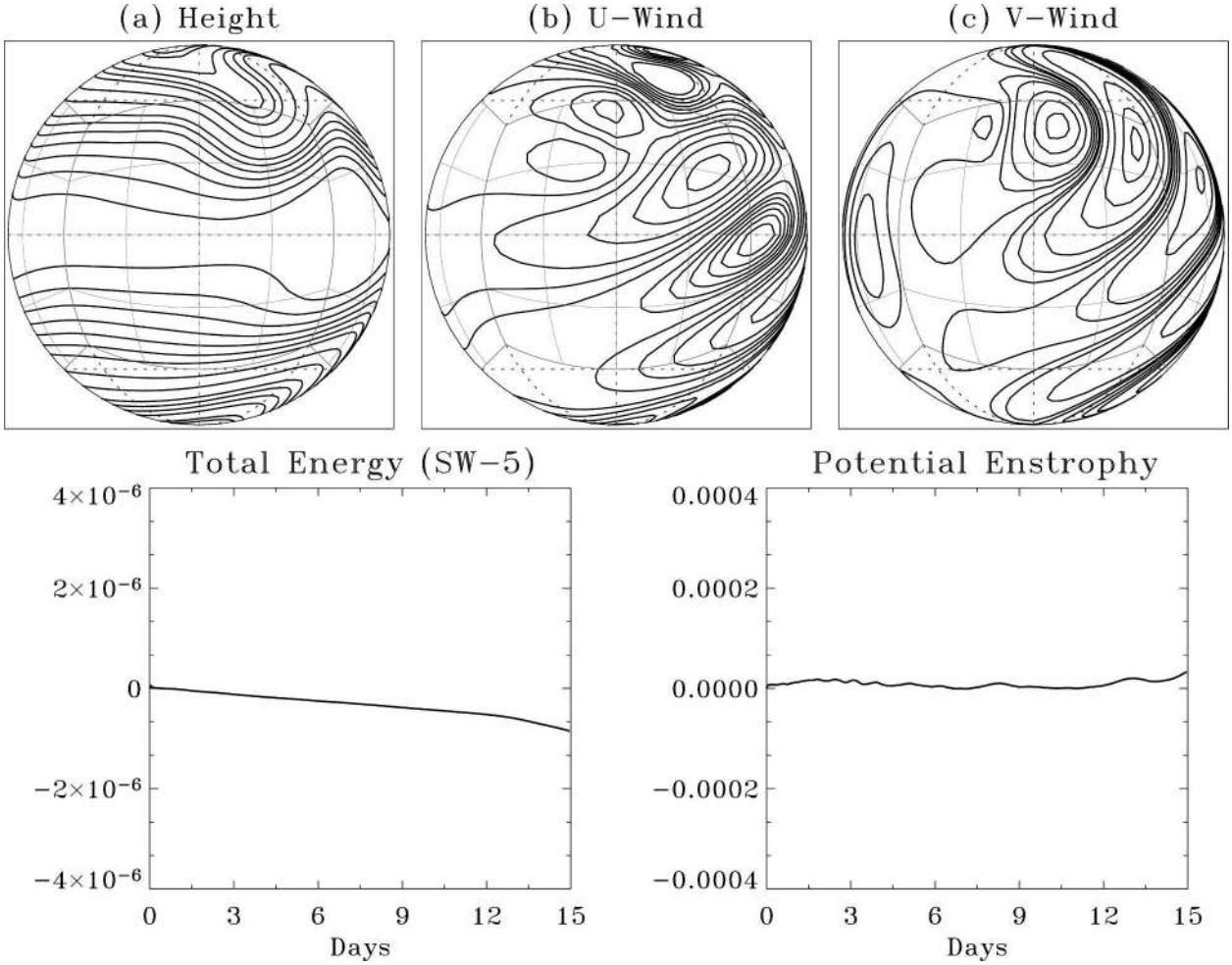

FIG. 6. (a) Numerical results for the SW test case 5 on a low-resolution grid with 54 elements ($N_e = 3$) and a high-order polynomial ($N = 8$). Contours of the (i) height, (ii) zonal, and (iii) meridional components of the velocity are shown after 10 days of integration, respectively. (b) Normalized time traces of (left) total energy and (right) potential enstrophy on the grid used in (a). The DG model was integrated for 15 days.

for both the wind and height fields for $N = 8$ (see their Fig. 8, p. 521); however, our results using fewer elements are completely smooth, as displayed in Fig. 6a.

Conservation of integral invariants can be monitored using the following normalized integral (W92):

$$\overline{\psi}(t) = \frac{I_g[\psi(\lambda, \theta, t)] - I_g[\psi(\lambda, \theta, 0)]}{I_g[\psi(\lambda, \theta, 0)]}, \qquad (18)$$

where I_g is the global surface integral as defined in W92. In the case of mass conservation $\psi = h$, for total energy $\psi = \{h\,\mathbf{v}\cdot\mathbf{v} + g[(h + h_s)^2 - h_s^2]\}/2$, and for potential enstrophy $\psi = (\zeta + f)^2/(2h)$. Discrete integrals in (18) are computed using an accurate GLL quadrature rule, and the values of $\overline{\psi}$ have been plotted as a function of time. Normalized discrete mass, energy, and potential enstrophy as a function time for a $864 \times 4 \times 4$ grid are shown in Fig. 5. In terms of total number of grid points, this grid provides a resolution somewhere between T42 and T63 of a global spectral model. Figure 5a clearly indicates that mass is conserved to machine precision. Exact conservation of mass for the DG method has been verified in the context of a pure advection test (solid-body rotation of a cosine bell) in NTL05; however, for the present study we use the full SW model for a nonlinear problem.

Note that the SW system (3)–(5) does not formally conserve the total energy or potential enstrophy, and it is interesting to observe how these invariants behave in the DG formulation. Figures 5b and 5c show the time evolution of total energy and potential enstrophy, respectively. There is a small gradual degradation in total energy from its initial value, but total potential enstrophy nearly remains constant. Even though the grid resolution used here is much lower than a T63 spectral model, conservation of total energy is much better than

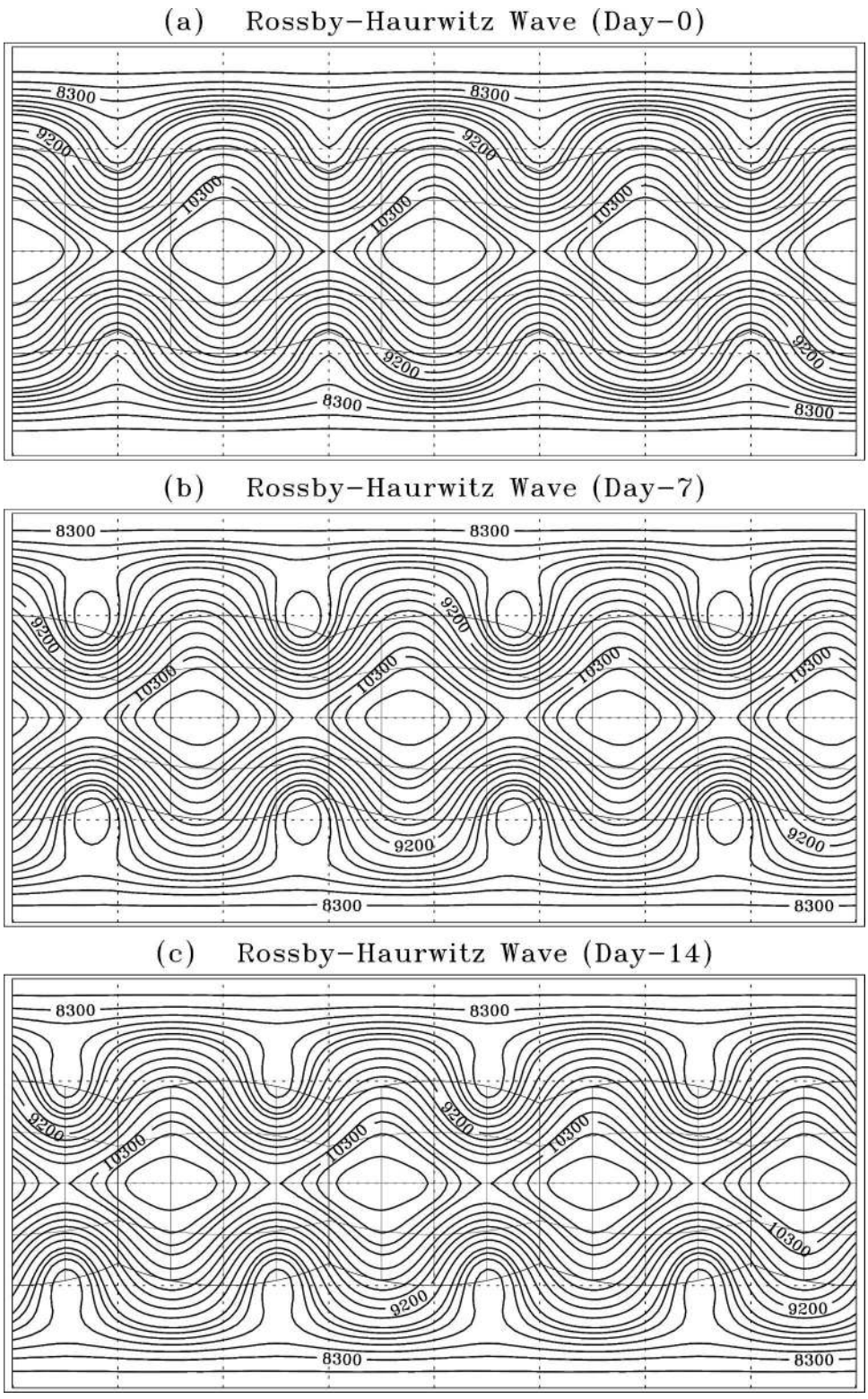

FIG. 7. Numerical results for SW test case 6 (Rossby–Haurwitz wave) on an 864 × 4 × 4 grid: (a) the initial height field and the simulated height fields at days (b) 7 and (c) 14, respectively.

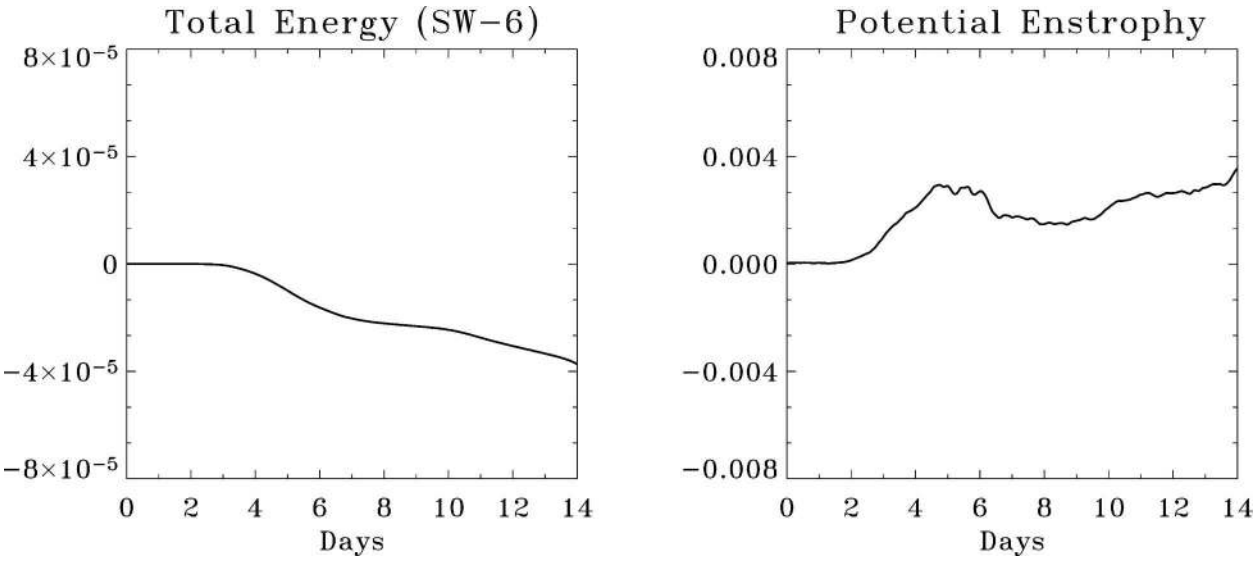

FIG. 8. Normalized time traces of (left) total energy and (right) potential enstrophy on a 486 × 4 × 4 grid, for the Rossby–Haurwitz wave. The DG model was integrated for 14 days.

that of the T63 spectral model (Jakob-Chien et al. 1995). When a *high-order* grid ($N = 8$) with a fewer number of elements ($M = 54$) is used, the conservation of total energy and potential enstrophy, as shown in Fig. 6b, are found to be comparable to that of the 864 × 4 × 4 *low-order* grid (Fig. 5). However, the high-order version uses only about 1/3 the number of points. Moreover, the energy and potential enstrophy errors are comparable or even better than the corresponding results reported by Thuburn (1997) with a finite-volume model that has roughly the resolution of a T100 spectral model.

c. Rossby–Haurwitz wave

The third experiment is test case 6 in W92, a zonal wavenumber-4 Rossby–Haurwitz wave. The initial state is an exact steadily propagating solution of the nondivergent barotropic vorticity equation, but not an exact solution of the full SW system.

Figure 7a shows the initial height field, and Figs. 7b and 7c show the numerical solution after 7 and 14 days of integration, respectively. We have used a 864 × 4 × 4 grid that gives resolution somewhere between T42 and T63 of a spectral model. Unlike the National Center for Atmospheric Research (NCAR) spectral model, the DG scheme does not employ any diffusion terms. The results shown in Fig. 7, after 7 and 14 days of integration, are strikingly similar to the reference solutions with a T213 spectral model (Jakob-Chien et al. 1995), both in phase and amplitude. To compare the results with a finite-volume model by Lin and Rood (1997) on a 128 × 64 grid (T42 resolution), we have chosen a low-resolution 486 × 4 × 4 grid (resolution less than a T42 spectral model). Figure 8 shows the evolution of total energy and potential enstrophy as a function of time for 14 days of integration for the Rossby–Haurwitz wave problem. The change in total energy is almost one order lower than Lin and Rood (1997), and the potential enstrophy error (from initial value) is of the same magnitude. As shown in Fig. 5, the potential enstrophy variation seems to have the tendency to change slowly; however, in Lin and Rood (1997) and Thuburn (1997), the corresponding plots deviate from the initial value at a more rapid rate.

d. Polar rotating low–high

The final experiment is the test proposed by McDonald and Bates (1989), simulating cross-polar flow with a geostrophically balanced initial state. There is no analytic solution for this problem. Recently Jablonowski (2004) and Giraldo et al. (2002) have employed this test. The initial fields consist of a low and high which are symmetrically located at the left and the right sides of the pole, respectively, when viewed from above. The low/high pattern rotates in the clockwise direction around the pole and after 10 days of integration the slightly deformed patterns return to the same (initial) locations.

The initial height and wind fields are given by

$$
\begin{aligned}
g\,h &= g\,h_0 + 2\omega a v_0 \sin^3\theta \cos\theta \sin\lambda \\
u &= -v_0 \sin\lambda \sin\theta\,(4\cos^2\theta - 1) \quad , \\
v &= v_0 \sin^2\theta \cos\lambda,
\end{aligned}
$$

where $gh_0 = 5.768 \times 10^4$ m^2 s^{-2}, and $v_0 = 20$ m s^{-1}. Note that the wind fields (u, v) are derived from height fields using the geostrophic relationship.

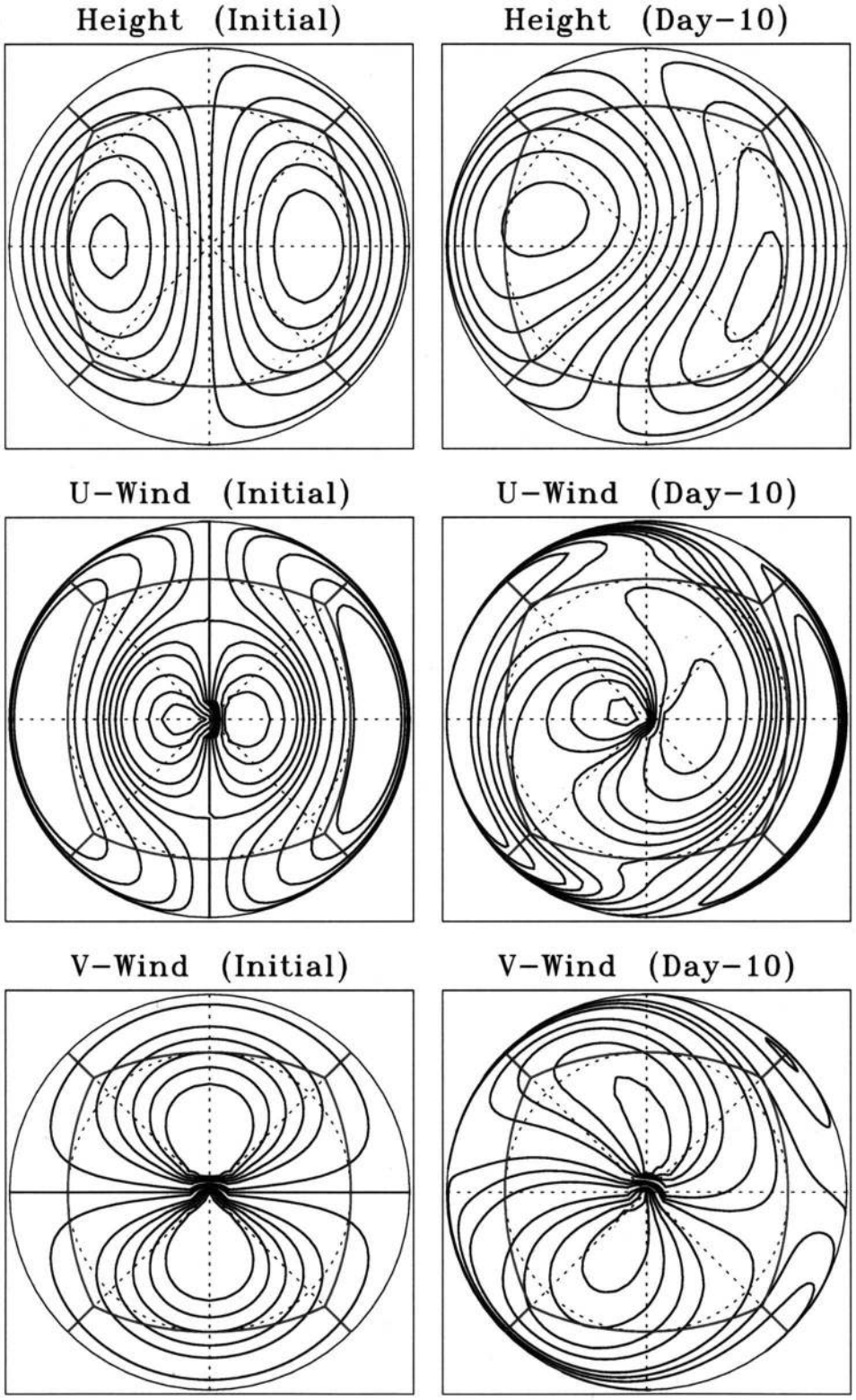

FIG. 9. Orthographic projection for the polar-rotating low–high problem. (left) Initial height and velocity components, from top to bottom, respectively. (right) Corresponding numerical solutions after 10 days of simulation.

Figure 9 shows the initial and numerical solutions for the height and wind fields. The DG model has been integrated for 10 days on a grid with 54 elements and $N = 8$. This configuration approximately matches the one used by Giraldo et al. (2002) in their test case 4, with 60 elements and $N = 8$. For this setup, Giraldo et al. (2002) reported "jagged" wind fields for their numerical simulations. However, Fig. 9 exhibits no such noise, and the u and v fields are smooth. We have repeated the experiments with higher values of N; however, the results are visibly indistinguishable and are not shown here.

5. Summary and conclusions

The discontinuous Galerkin (DG) transport scheme proposed by Nair et al. (2005) has been further extended to the full set of nonlinear flux form shallow water equations on the sphere. The computational domain is the cubed sphere, where a sphere is decomposed into six identical regions obtained by central (gnomonic) equiangular projections of the faces of the inscribed cube onto the spherical surface. The DG discretization employs a modal basis set consisting of Legendre polynomials, and fluxes along the boundaries of the elements (internal interfaces) are approximated by a Lax–Friedrichs scheme. A third-order total variation diminishing (TVD) Runge–Kutta scheme has been used for time integration, without any filter or limiter. The model has been evaluated using the standard test suite proposed by Williamson el al. (1992).

The DG scheme exhibits exponential convergence for SW test case 2 (steady-state geostrophic flow problem). The DG solutions to the SW test cases are much better than those of a spectral model (Jakob-Chien et al. 1995) for a given spatial resolution. Even with high-order spatial discretization, the solutions do not exhibit spurious oscillations for the flow over a mountain test case. Conservation of integral invariants has also been compared with existing finite-volume models (e.g., Lin and Rood 1997; Thuburn 1997). Our model conserves mass to machine precision, and although the scheme does not formally conserve global invariants such as total energy and potential enstrophy, conservation of these quantities is better preserved than in lower-order finite-volume models. An efficient slope limiter is under development and results will be communicated in the near future. Parallel implementation of the DG model in the Scientific Computing Division (SCD)/NCAR SE modeling framework (Loft et al. 2001) is also in progress.

APPENDIX

Flux Jacobians for the Shallow Water System

Consider the flux form shallow water system (6), and the flux function in x^1 direction expressed as $\mathbf{F}_1(\mathbf{q})$ with $\mathbf{q} \equiv [\sqrt{G}h, u_1, u_2]^{\mathrm{T}} = [q_1, q_2, q_3]^{\mathrm{T}}$. Then the flux Jacobian in x^1 direction is defined to be $\mathbf{F}_1'(\mathbf{q})$ (for details, see Leveque 2002). The flux function $\mathbf{F}_1 = [\sqrt{G}h\, u^1, \Phi + \tfrac{1}{2}(u_1u^1 + u_2u^2), 0]^{\mathrm{T}}$ can be expressed in covariant form using the metric defined in (1), and the result can be further expressed in terms of $\mathbf{q}$ as given below:

$$\mathbf{F}_1(\mathbf{q}) = \begin{bmatrix} q_1(G^{11}q_2 + G^{12}q_3) \\ G^*q_1 + \dfrac{1}{2}[q_2(G^{11}q_2 + G^{12}q_3) + q_3(G^{21}q_2 + G^{22}q_3)] \\ 0 \end{bmatrix}, \tag{A1}$$

where $G^*q_1 = gh = \Phi$. The flux Jacobian in x^1 direction is given by

$$\mathbf{F}_1'(\mathbf{q}) = \frac{d}{d\mathbf{q}}\mathbf{F}_1(\mathbf{q}) = \begin{bmatrix} G^{11}q_2 + G^{12}q_3 & G^{11}q_1 & G^{12}q_1 \\ G^* & G^{11}q_2 + \overline{G}q_3 & G^{22}q_3 + \overline{G}q_3 \\ 0 & 0 & 0 \end{bmatrix}, \tag{A2}$$

where $\overline{G} = (G^{12} + G^{21})/2$. Eigenvalues ($\lambda_e$) of the system (A2) are obtained from the characteristic equation $|\mathbf{F}'(\mathbf{q}) - \lambda_e\mathbf{I}| = 0$ leading to the following quadratic equation in λ_e:

$$(G^{11}q_2 + G^{12}q_3 - \lambda_e)(G^{11}q_2 + \overline{G}q_3 - \lambda_e) = G^*G^{11}q_1,$$

with roots

$$\lambda_e = G^{11}u_1 + \frac{1}{2}(G^{12} + \overline{G})u_2 \pm \frac{1}{2}[(G^{12} - \overline{G})^2u_2^2 + 4\Phi G^{11}]^{1/2}. \tag{A3}$$

For the metric tensor G_{ij} defined in (1), we have $G^{12} = G^{21} = \overline{G}$; therefore (A3) takes the following simple form:

$$\lambda_e = (G^{11}u_1 + G^{12}u_2) \pm \sqrt{\Phi\, G^{11}} = u^1 \pm \sqrt{\Phi\, G^{11}}. \tag{A4}$$

Because we are looking for the maximum value of the flux Jacobian α in the numerical flux Eq. (10), we have

$$\alpha^1 = \lambda_{\max} = \max(|u^1| + \sqrt{\Phi G^{11}}). \tag{A5}$$

Similarly, the flux Jacobian in the x^2 direction is given by $\mathbf{F}_2'(\mathbf{q})$, and the corresponding maximum eigenvalue for α in (10) can be derived as below:

$$\alpha^2 = \max(|u^2| + \sqrt{\Phi G^{22}}). \tag{A6}$$

REFERENCES

Arakawa, A., and V. R. Lamb, 1981: A potential enstrophy and energy conserving scheme for the shallow-water equations. *Mon. Wea. Rev.,* **109,** 18–36.

Bacon, D. P., and Coauthors, 2000: A dynamically adapting weather and dispersion model: The Operational Multiscale Environment Model with Grid Adaptivity (OMEGA). *Mon. Wea. Rev.,* **128,** 2044–2076.

Bassi, F., and S. Rebay, 1997: A high-order accurate discontinuous finite element solution of the 2D Euler equations. *J. Comput. Phys.,* **138,** 251–285.

Cockburn, B., and C. W. Shu, 1989: TVB Runge–Kutta local projection discontinuous Galerkin method for conservation laws II: General framework. *Math. Comput.,* **52,** 411–435.

——, and ——, 1998: The Runge–Kutta discontinuous Galerkin finite element method for conservation laws V: Multidimensional systems. *J. Comput. Phys.,* **141,** 199–224.

——, and ——, 2001: The Runge–Kutta discontinuous Galerkin method for convection-dominated problems. *J. Sci. Comput.,* **16,** 173–261.

——, G. E. Karniadakis, and C. W. Shu, 2000: *Discontinuous Galerkin Methods: Theory, Computation, and Applications*. Lecture Notes in Computational Science and Engineering, Vol. 11, Springer-Verlag, 470 pp.

Fournier, A., M. A. Taylor, and J. J. Tribbia, 2004: A spectral element atmospheric model (SEAM): High-resolution parallel computation and localized resolution of regional dynamics. *Mon. Wea. Rev.,* **132,** 726–748.

Giraldo, F. X., and T. E. Rosmond, 2004: A scalable spectral element Eulerian atmospheric model (SEE-AM) for NWP: Dynamical core test. *Mon. Wea. Rev.,* **132,** 133–153.

——, J. S. Hesthaven, and T. Warburton, 2002: Nodal high-order discontinuous Galerkin methods for spherical shallow water equations. *J. Comput. Phys.,* **181,** 499–525.

Gottlieb, S., C. W. Shu, and E. Tadmor, 2001: Strong stability-preserving high-order time discretization methods. *SIAM Rev.,* **43,** 89–112.

Heikes, R., and D. A. Randall, 1995: Numerical integration of the shallow water equations on a twisted icosahedral grid. Part I: Basic design and results of tests. *Mon. Wea. Rev.,* **123,** 1862–1880.

Iskandrani, M., D. B. Haidvogal, J. C. Levin, E. Curchister, and C. A. Edwards, 2002: Multiscale geophysical modeling using the spectral element method. *Comput. Sci. Eng.,* **4,** 42–48.

Jablonowski, C., 2004: Adaptive grids in weather and climate modeling. Ph.D. thesis, University of Michigan, 272 pp.

Jakob-Chien, R., J. J. Hack, and D. L. Williamson, 1995: Spectral transform solutions to the shallow water test set. *J. Comput. Phys.,* **119,** 164–187.

Karniadakis, G. E., and S. J. Sherwin, 1999: *Spectral/hp Element Methods for CFD.* Oxford University Press, 390 pp.

Leveque, R. J., 2002: *Finite Volume Methods for Hyperbolic Problems*. Cambridge Texts in Applied Mathematics, Cambridge University Press, 558 pp.

Lin, S.-J., and B. Rood, 1997: An explicit flux-form semi-Lagrangian shallow water model on the sphere. *Quart. J. Roy. Meteor. Soc.,* **123,** 2531–2533.

Loft, R. D., S. J. Thomas, and J. M. Dennis, 2001: Terascale spectral element dynamical core for atmospheric general circulation models. *Proc. ACM/IEEE Supercomputing 2001 Conf.,* Denver, CO, ACM/IEEE, CD-ROM.

McDonald, A., and J. R. Bates, 1989: Semi-Lagrangian integration of a shallow water model on the sphere. *Mon. Wea. Rev.,* **117,** 130–137.

Nair, R. D., S. J. Thomas, and R. D. Loft, 2005: A discontinuous Galerkin transport scheme on the cubed sphere. *Mon. Wea. Rev.,* **133,** 827–841.

Rančić, M. R., J. Purser, and F. Mesinger, 1996: A global-shallow water model using an expanded spherical cube. *Quart. J. Roy. Meteor. Soc.,* **122,** 959–982.

Remacle, J.-F., J. E. Flaherty, and M. S. Shephard, 2003: An adaptive discontinuous Galerkin technique with an orthogonal basis applied to compressible flow problems. *SIAM Rev.,* **45,** 53–72.

Ronchi, C., R. Iacono, and P. S. Paolucci, 1996: The "cubed sphere": A new method for the solution of partial differential equations in spherical geometry. *J. Comput. Phys.,* **124,** 93–114.

Sadourny, R., 1972: Conservative finite-difference approximations of the primitive equations on quasi-uniform spherical grids. *Mon. Wea. Rev.,* **100,** 136–144.

Taylor, M., J. Tribbia, and M. Iskandrani, 1997: The spectral element method for the shallow water equations on the sphere. *J. Comput. Phys.,* **130,** 92–108.

Thomas, S. J., and R. D. Loft, 2002: Semi-implicit spectral element model. *J. Sci. Comput.,* **17,** 339–350.

Thuburn, J., 1997: A PV-based shallow-water model on a hexagonal-icosahedral grid. *Mon. Wea. Rev.,* **125,** 2328–2336.

Williamson, D. L., J. B. Drake, J. Hack, R. Jakob, and P. N. Swartztrauber, 1992: A standard test set for numerical approximations to the shallow water equations in spherical geometry. *J. Comput. Phys.,* **102,** 211–224.